IEEE Open Journal of
Industry Applications

Received 28 August 2022; revised 2 December 2022, 18 December 2022, and 1 January 2023; accepted 11 January 2023. Date of publication 18 January 2023; date of current version 1 February 2023. The review of this article was arranged by Associate Editor Mauro Di Nardo.

Digital Object Identifier 10.1109/OJIA.2023.3236984

Experimental Verification of Passive Axial Electrodynamic Suspension in a Bearingless Motor

GUILHERME CAVALCANTE RUBIO, VISHNU C. HOTHUR KOMAL, YUSUKE FUJII, AND AKIRA CHIBA

Department of Electrical and Electronic Engineering, Tokyo Institute of Technology, Tokyo 152-8550, Japan

CORRESPONDING AUTHOR: GUILHERME CAVALCANTE RUBIO (e-mail: gcavrubio@gmail.com)

This work was supported by the JSPS under Grant 19H00759.

ABSTRACT This article investigates a bearingless motor with passive electrodynamic axial suspension. The axial suspension force is generated by a specific coil configuration called a figure-eight coil. Radial directions and tilting angles are stabilized by passive permanent magnet bearings. Since axial electrodynamic force increases with rotational speed, it must overcome a certain minimum threshold speed to compensate for the rotor weight and the unstable axial force caused by the permanent magnet bearing. Theoretical equations are derived for the braking torque caused by the suspension current and for the steady-state axial equilibrium position at constant rotational speed. A method based on the braking torque equation is proposed for correcting the mismatch between the magnetic center of the bearingless motor and the middle point of the axial clearance. This method sets the middle point between upper and lower touchdown positions in the same place where the motor current is minimum during passive axial suspension. Axial suspension is confirmed in the experiment with a noncontact laser sensor.

INDEX TERMS Bearingless, electrodynamic, magnetic levitation, passive suspension, permanent magnet, permanent magnet synchronous machine, surface permanent magnet.

I. INTRODUCTION

Some applications of electric machines, such as blood pumps and high-speed drives, require durable and reliable devices. Usually, rotating electric machines are supported by mechanical ball bearings. Those bearings wear due to friction and demand regular preventive maintenance. It is possible to reduce friction by substituting the mechanical ball bearings by magnetic forces.

Either active control or passive stabilization can be used to achieve noncontact magnetic suspension. If the shaft position is completely regulated by active magnetic forces, it is said that 5 degrees of freedom (5DOF) are actively controlled [1]. The radial direction, tilting angle, and axial position are regulated by a feedback control system. The 5DOF suspension strategy requires several position sensors and inverters, adding significant costs and complexity due to suspension control. By combining passive techniques with active position control, it is possible to achieve full noncontact suspension with fewer actively regulated DOF. There are several examples of 2DOF [2], [3], [4], [5] and 1DOF [6], [7], [8], [9] actively positioned bearingless motors in the literature. According to the Earnshaw theorem, it is not possible to achieve full passive suspension only through permanent magnet bearings in static state [10]. However, it is possible to combine permanent magnet bearings with other passive suspension techniques, such as hydrodynamic bearings [10], superconductor levitation [11], gyroscopic effects [12], diamagnetic materials at room temperature [13], and electrodynamic forces generated by eddy currents. Among these passive suspension techniques, electrodynamic suspension was chosen for this project, because the motor coils that generate torque are also used for passive stabilization, they provide stronger stiffness than that of room temperature diamagnetic levitation, and they do not require superconductors with a dedicated cooling system. The electrodynamic suspension principle was already employed in several electrodynamic bearings [14], [15], [16], [17], [18],

[19], [20], [21], [22] and bearingless motors [23], [24], [25], [26], [27], [28], [29], [30], [31], [32], [33], [34], [35]. Full passive suspension was confirmed in a bearingless motor that combines axial electrodynamic suspension and radial permanent magnet bearings [29], [30], [31]. However, the rotor remains in axial touchdown position until a certain minimum rotational speed is surpassed. In case full suspension is required for all rotational speeds, it is possible to operate these bearingless motors as a single-drive 1DOF machine up to the threshold speed of axial suspension [30], [35].

This article presents a surface-mounted permanent magnet bearingless motor with axial electrodynamic suspension [32], [33], [34], [35]. The radial directions and tilting angles are stabilized by radial permanent magnet bearings. The axial electrodynamic force is proportional to the axial displacement and increases with rotational speed. This principle is based on the lift and guidance coils applied in the Japan railway high-speed maglev train [36], [37], [38], [39]. By arranging the stator coils in a pattern that resembles the number eight (8), a stabilizing suspension current is induced when the rotor is axially displaced. This principle was previously adapted for bearingless motors [23], [28], but, owing to the lack of superconducting electromagnets, flux density and electrodynamic forces are considerably lower than that of the maglev train for high-speed transportation. The machine covered in this article has a double rotor structure with three layers of permanent magnets [33], [34], [35] for improved radial flux density and passive axial electrodynamic force. This radial air-gap rotor shape offers the possibility of axial suspension with 1DOF control at low rotational speed. The rotor is made axially asymmetric by removing one of the outer layers of permanent magnets [35]. This asymmetric topology allows simple commutation between the active and passive suspension modes by turning OFFthe suspension control loop without any physical switching.

It includes the improvements of a bearingless motor with axial electrodynamic suspension. Experimental results up to 8065 r/min are shown, instead of the 5000 r/min limit considered in [34], making it possible to confirm axial suspension without additional support structures for weight relief. A method based on the relation between the braking torque and the axial position is proposed to minimize mismatches between the magnetic center of the permanent magnets and the center of axial mechanical clearance. This method finds the origin of the axial displacement z by second-degree fitting of rms motor currents measured with an oscilloscope. Axial suspension was confirmed in the experiment by a noncontact laser sensor.

Throughout this article, finite element analysis (FEA) and theoretical equations are shown. They are used to estimate the braking torque due to suspension current and the minimum rotational speed that is required to achieve axial electrodynamic suspension. For stable axial suspension, the axial electrodynamic stiffness must be higher than the unstable axial stiffness generated by the radial permanent magnet bearings. Moreover, to lift the rotor from touchdown condition, the electrodynamic force must be higher than the sum of the rotor weight and the repulsive axial force by the permanent magnet bearings. This repulsive force is proportional to axial displacement. Thus, the minimum force required for suspension also depends on the axial touchdown position.

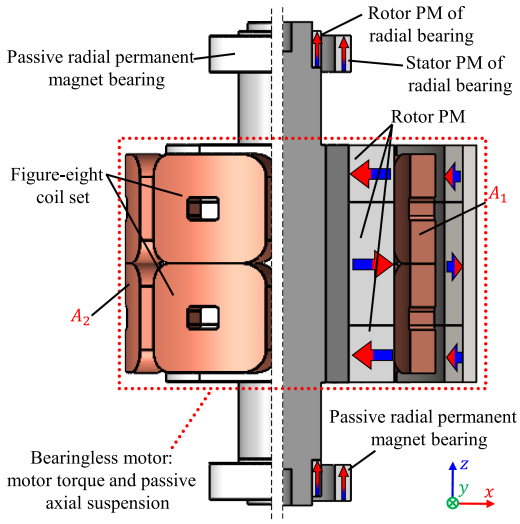

FIGURE 1. Simplified 3-D model of the bearingless motor with electrodynamic axial suspension. Interaction between rotor permanent magnets and induced currents in the stator generates passive axial forces that increase with rotational speed and axial displacement. Radial permanent magnet bearings stabilize the radial position and tilting.

II. AXIAL ELECTRODYNAMIC SUSPENSION PRINCIPLE

A. DESCRIPTION OF THE MACHINE

Fig. 1 shows a simplified 3-D model of the bearingless motor and the radial permanent magnet bearings. A front view and a section cut of the machine are shown side by side. This machine is a permanent magnet synchronous motor with concentrated rectangular coreless coils. The stator coils are divided into two layers. Coils in the upper layer are connected in parallel association with the coil directly below. Each of these pairs is called a figure-eight coil set, owing to their shape that resembles the number eight. The rotor has three layers of four-pole permanent magnets. The permanent magnets in the upper and lower layers are polarized in an opposite direction to that of the central permanent magnet layer. The rotor has an outer and inner parts connected by an aluminum frame; however, for better visualization, it is omitted in Fig. 1. Permanent magnets in the outer part have their magnetic poles aligned with those in the inner part [33].

There are two pairs of permanent magnet rings positioned at both ends of the rotor shaft. In each pair, one permanent magnet is attached to the rotor shaft and the other one is mounted on the stator side. Owing to the magnetic pole configuration of these pairs, there are repulsive forces between the rotor and stator. These repulsive forces centralize the shaft in the radial direction and prevent tilting. On the other hand, they also repel the rotor shaft along the axial direction, also known as thrust direction, causing axial instability. To achieve stable axial suspension, the unstable axial stiffness by the radial permanent magnet bearings must be compensated for by the axial electrodynamic stiffness.

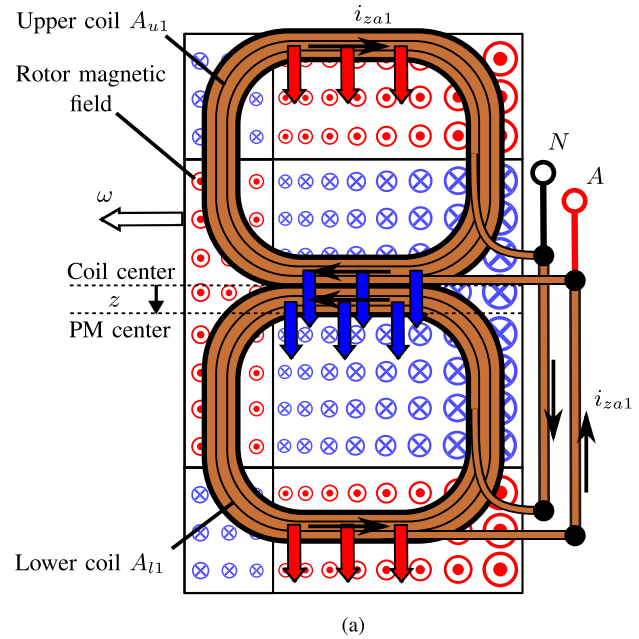

FIGURE 2. Figure-eight coil A_1 connected to phase A. The figure-eight configuration is achieved by connecting the upper coil A_{u1} and the lower coil A_{l1} in parallel association. (a) Path of the suspension current i_{za1} inside a planar view of the figure-eight coil A_1. (b) Path of the motor current i_a inside a planar view of the figure-eight coil A_1

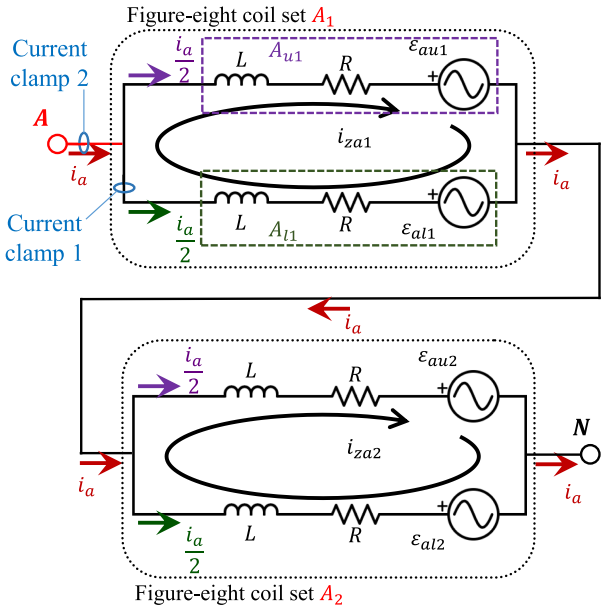

FIGURE 3. Equivalent circuit of the figure-eight coil sets A_1 and A_2.

an imbalance between back-electromotive forces (back-EMF) in the upper and lower coils generates a circulating current i_{za1}. When i_{za1} flows in the counter-clockwise direction in the upper coil, it flows in the clockwise direction in the lower coil, and vice versa. Interaction between i_{za1} and the magnetic field crossing the horizontal coil segments results in Lorentz forces along the axial direction. Those forces push the rotor and stator back to the central axial position.

Fig. 2(b) shows the path of an external motor current i_a supplied by an inverter. A Lorentz force is generated along the vertical segments of the figure-eight coil set. The motor torque is, thus, actively regulated by the q-axis component of i_a. The figure-eight coil set A_1 is connected in series with the coil set A_2 in the opposite side of the stator, as shown in Fig. 3. Assuming that the upper and lower coils have the same impedance value, the current i_a divides itself equally between the upper and lower paths. It should be noted that the external motor current $i_a/2$ flows in the same direction in the upper and lower coils. It is the opposite of what happens to the suspension current i_{za1}. Since forces generated along the horizontal coil segments cancel each other, it is not possible to regulate the axial suspension force through the direct axis component of i_a.

B. AXIAL ELECTRODYNAMIC STIFFNESS

The equation for the axial electrodynamic stiffness was derived in the authors' previous article [33]. This section highlights the equations that are most relevant for this article.

The upper and lower coils, A_{u1} and A_{l1}, respectively, are assumed to have identical shape, resistance R, and self-inductance L. Mutual inductance between coils is neglected. This is assumed because the stator is coreless and the winding is concentrated. An FEA confirmed that the highest mutual inductance between neighbor coils corresponds to about 4%

Fig. 2(a) shows a planar representation of the figure-eight coil A_1 connected to the phase A terminal. It consists of the upper and lower coils A_{u1} and A_{l1}, respectively, connected in parallel. It is assumed that the magnetic flux density distribution is sinusoidal along the angular direction. The magnetic field generated by the rotor permanent magnets is represented by the red vectors, coming out of the sheet plane, and the blue vectors, entering the sheet plane. When the rotor is displaced from the central axial position $z = 0$,

of their self-inductances. The rotor rotates at a constant mechanical rotational angular speed ω and is radially centralized. Magnetic flux linkages in the upper and lower coils, λ_{au1} and λ_{al1}, respectively, are derived as

$$\begin{cases} \lambda_{au1} = (\lambda_0 + K_\lambda\, z)\cos(p\omega t) \\ \lambda_{al1} = (\lambda_0 - K_\lambda\, z)\cos(p\omega t) \end{cases} \tag{1}$$

where K_λ is the ratio of flux linkage variation in terms of axial position z. It is a constant that depends on the peak magnetic flux density, number of turns per coil, and coil shape [33]. The constant λ_0 is the flux amplitude when $z = 0$, p is the number of pole pairs, and t is the time variable.

The back-EMF in the upper and lower coils, ε_{au1} and ε_{al1}, respectively, are derived from (1) as

$$\begin{cases} \varepsilon_{au1} = \dfrac{d\lambda_{au1}}{dt} = p\omega(-K_\lambda\, z - \lambda_0)\sin(p\omega t) \\ \varepsilon_{al1} = \dfrac{d\lambda_{al1}}{dt} = p\omega(K_\lambda\, z - \lambda_0)\sin(p\omega t). \end{cases} \tag{2}$$

Assuming that the upper and lower coils are connected in parallel association, the steady-state suspension current i_{za1} is derived in terms of rotational speed ω and axial position z as

$$i_{za1} = \frac{p\omega K_\lambda z}{\sqrt{R^2 + (p\omega L)^2}}\sin(p\omega t - \theta_c) \tag{3}$$

where θ_c is the impedance angle of the coils, that is, the arcsin of the ratio from the inductive reactance to coil impedance. The angle θ_c, in radians, is derived as

$$\theta_c = \arcsin\left(\frac{p\omega L}{\sqrt{R^2 + (p\omega L)^2}}\right). \tag{4}$$

If the rotor is axially centered, that is, $z = 0$, thus, i_{za1} is zero; otherwise, $z \neq 0$ results in a circulating suspension current i_{za1}.

Interaction between the suspension current i_{za1} and the magnetic field by the rotor permanent magnets results in Lorentz forces on the stator coils. Defining F_{zeT} as the total force on the six figure-eight coil sets, the axial electrodynamic stiffness k_{ze} is derived from the projection of F_{zeT} on the rotor side as

$$k_{ze} = -\left(-\frac{\partial F_{zeT}}{\partial z}\right) = \frac{c\, K_\lambda^2\, p^2\omega^2\, L}{R^2 + p^2\omega^2\, L^2} \tag{5}$$

where c is the number of figure-eight coil sets.

Table 1 gives the parameters of (5). The resistance R was directly measured on the coils. The average resistance of individual coils is 2.6 Ω. The self-inductance L was calculated using a single-step 3-D FEA as 1.03 mH. It is numerically equal to the magnetic flux linked by the coil A_{u1} when fed by a 1 A current dc while all other coils have open terminals and the permanent magnets are suppressed. The constant K_λ was obtained by calculating the flux linked by coil A_{u1} at several constant axial positions z using a 3-D FEA during one electric cycle. A third harmonic component is present in the flux waveform, owing to the parallel magnetization of the rotor permanent magnets. The amplitude of the flux linkage,

TABLE 1. Parameters Used in (5)

Parameter	Symbol	Value	Assessment method
Resistance	R	2.6 Ω	Experimental measurement
Inductance	L	1.03 mH	FEA
Ratio from flux variation to axial displacement (fundamental)	K_λ	5.5 Wb/m	FEA
Ratio from flux variation to axial displacement (third harmonic)	$K_{\lambda 3}$	0.5 Wb/m	FEA

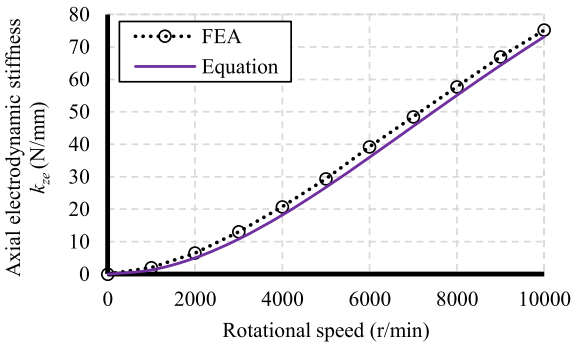

FIGURE 4. Finite element analysis results and theoretical calculations of axial electrodynamic stiffness.

equivalent to $\lambda_0 + K_\lambda\, z$, was obtained through fast Fourier transform. The third harmonic component generates a small contribution to the axial stiffness [27]. The figure-eight coil connection is modeled by connecting the upper and lower coils in parallel association in the equivalent circuit of the FEA study. Rotational speed and axial position are constant for each simulation case. No linear approximations are assumed, including the back-iron yoke. The constant K_λ was calculated through first degree fitting as 5.5 and 0.5 Wb/m for the fundamental and third harmonic components, respectively. The third harmonic contributes with 1.7% of the total theoretical axial stiffness at 10 000 r/min.

Fig. 4 shows a comparison between the electrodynamic axial stiffness k_{ze} calculated using a 3-D FEA along one electrical cycle and the results yielded by (5). Rotational speed and axial position are constant for each simulation case. The coil resistances in the FEA were set to 2.6 Ω. Discrepancy of 3.1% is observed between the FEA results and the equation at 10 000 r/min. This small difference is probably caused by the mutual inductances that were neglected in the derivation process [33]. More accurate theoretical modeling might be possible considering the mutual inductances [26].

C. BRAKING TORQUE DUE TO SUSPENSION CURRENT

Assuming that the machine rotates at constant speed in a no-load state, it is possible to estimate the braking torque due to the suspension currents by dividing its respective power losses by the mechanical rotational angular speed ω in rad/s [21].

As derived in (3), the amplitude of the circulating suspension current in the figure-eight coil is proportional to the axial displacement z and increases with rotational speeds when

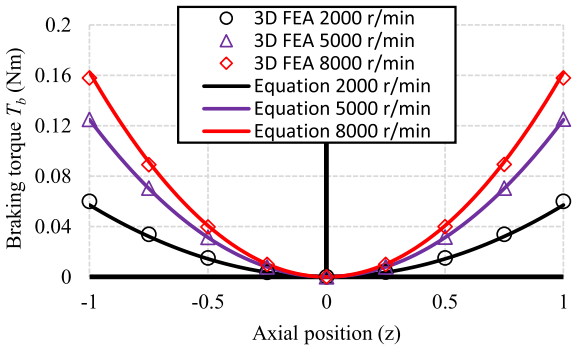

FIGURE 5. Finite element analysis results and theoretical calculations of braking torque.

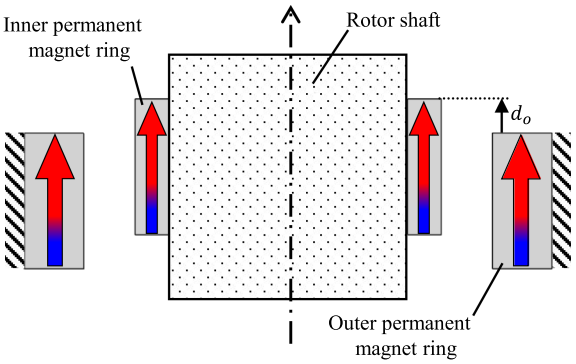

FIGURE 6. Radial permanent magnet bearing.

$\omega \ll R/pL$. The suspension current generates power losses in the figure-eight coil resistance. Defining the suspension rms current I_{za1}, neglecting the harmonic components, the total power loss P_z in a stator with c figure-eight coil sets is derived from (3) as

$$P_z = 2cRI_{za1}^2 = cR\frac{(p\omega K_\lambda z)^2}{R^2 + (p\omega L)^2}. \tag{6}$$

The braking torque is derived from (6) as

$$T_b = \frac{P_z}{\omega} = cR\omega\frac{(pK_\lambda z)^2}{R^2 + (p\omega L)^2}. \tag{7}$$

It is concluded from (6) and (7) that both the power loss and the braking torque due to the axial suspension current are proportional to the square of axial displacement z.

Fig. 5 shows a comparison between results yielded by (7) and FEA calculations of Lorentz torque in the coils. The markers represent the FEA results, whereas full lines represent the equation results. There is a good correspondence between both results.

III. RADIAL PERMANENT MAGNET BEARINGS AND REQUIREMENTS FOR AXIAL SUSPENSION

A. STABILIZING PASSIVE RADIAL STIFFNESS

The electrodynamic suspension principle employed in this machine stabilizes the rotor shaft in the axial direction. Passive radial permanent magnet bearings are used to stabilize the radial direction and tilting angle of the shaft. There are two of those, one mounted on the upper end and another mounted on the lower end of the rotor shaft. Fig. 6 shows a radial permanent magnet bearing. The inner permanent magnet ring is mounted on the rotor shaft. The outer ring is mounted on the structure frame. The magnets are assembled in a repulsive configuration.

The repulsive force between the magnet rings stabilizes the radial direction, but it also destabilizes the axial direction. In this configuration, the unstable axial stiffness k_{zp} is twice as high as the stable radial stiffness k_{rp}[10], that is,

$$k_{zp} = -2k_{rp}. \tag{8}$$

A positive stiffness indicates a stabilizing force, whereas a negative stiffness indicates a destabilizing force. This relation is valid for static permanent magnets in the absence of soft magnetic materials and with small displacements.

For the axial shaft position to become stable, the electrodynamic axial stiffness k_{ze} by the figure-eight coils must compensate for the destabilizing axial stiffness k_{zp} by the two permanent magnet bearings, satisfying the following condition:

$$2k_{zp} + k_{ze} > 0. \tag{9}$$

Equations (8) and (9) indicate that the minimum electrodynamic stiffness increases with the radial stiffness of the permanent magnet bearings. Therefore, the stabilizing radial stiffness k_{rp} should be as low as possible. As for a permanent magnet machine with an iron core stator, there are magnetic pull forces between the rotor and stator that cause radial instability. In that case, the minimum k_{rp} can be specified to compensate for that unstable radial stiffness. On the other hand, the machine presented in this article has coreless stator; therefore, there are no static magnetic pull forces in the radial direction. For this reason, the radial stiffness k_{rp} did not have a minimum specification and was arbitrarily chosen.

B. CONDITIONS FOR AXIAL SUSPENSION

The minimum rotational speed to achieve axial suspension with a certain radial permanent magnet bearing can be estimated with the support of FEA.

Fig. 6 shows an axial offset d_o between the permanent magnets mounted on the rotor and stator. This is the rated displacement when the motor permanent magnets are aligned with the center of the figure-eight coils, that is, $z = 0$. Considering the offset d_o, the axial force F_{zp}, resultant from both radial permanent magnets, is derived as

$$F_{zp} = -2k_{zp}(z + d_o) = F_o - 2z\,k_{zp} \tag{10}$$

where $F_o = -2d_o\,k_{zp}$. The force F_o is adjusted to partially compensate for the rotor weight. By relieving part of the axial load on the shaft, the minimum electrodynamic stiffness requirement for achieving axial suspension is reduced as well. Assuming a constant rotational speed, defining the rotor mass m and the acceleration of gravity g, at steady-state equilibrium condition, resultant axial force on the suspended rotor is zero,

TABLE 2. Characteristics of the Permanent Magnet Rings Used in the Passive Radial Bearing

Identification	Inner diam.	Outer diam.	Height	Grade
Outer PM	24 mm	31 mm	8 mm	N42SH
Inner PM	14 mm	18 mm	8 mm	N40

implying the condition

$$0 = F_o - mg - z\,(k_{ze} + 2k_{zp}) \tag{11}$$

where $k_{ze} + 2k_{zp} > 0$ indicates the condition for a stable axial stiffness. The minimum electrodynamic stiffness for achieving axial suspension is derived by solving (11) at the lower axial touchdown position $z = z_t$

$$k_{ze} > \frac{F_o - mg}{z_t} - 2k_{zp} \tag{12}$$

where $k_{zp} < 0$, $k_{ze} > 0$, and $z_t < 0$. When the rotational speed increases, so does the electrodynamic stiffness k_{ze}. When k_{ze} overcomes the minimum value of condition (12), the steady-state axial equilibrium position z_b of the suspended rotor is derived from (11) as

$$z_b = \frac{F_o - mg}{k_{ze} + 2k_{zp}}. \tag{13}$$

The steady-state equilibrium position z_b can be calculated in terms of the rotational speed ω by substituting (5) into (13)

$$z_b = \frac{F_o - mg}{\dfrac{c\,K_\lambda^2\,p^2\omega^2\,L}{R^2 + p^2\omega^2\,L^2} + 2k_{zp}}. \tag{14}$$

The limit steady-state equilibrium position z_b for very high rotational speeds is derived from (14) as

$$\lim_{\omega\to\infty} z_b = \frac{F_o - mg}{\dfrac{c\,K_\lambda^2}{L} + 2k_{zp}}. \tag{15}$$

At steady-state full passive suspension, the higher the electrodynamic stiffness, the lower the absolute value of the axial displacement. However, z_b approaches (15) as the rotational speed approaches infinity. If a steady-state equilibrium position close to $z_b = 0$ is desired, the axial displacement between permanent magnets in the radial bearing must be carefully adjusted to have F_o as close as possible to the weight force.

C. ESTIMATION OF THE MINIMUM ROTATIONAL SPEED TO ACHIEVE AXIAL SUSPENSION

Table 2 summarizes the dimensions and grades of the neodymium permanent magnets employed in the radial permanent magnet bearings.

The unstable axial stiffness k_{zp} was measured with a six-axis force sensor. The outer permanent magnet was fixed to the sensor. The inner permanent magnet was radially centralized with the outer ring. The distance between both rings was adjusted during the experiment in steps of 0.2 mm. The axial force was measured for several axial displacements and k_{zp} was estimated through first-degree fitting as $k_{zp} = -5.66$ N/mm.

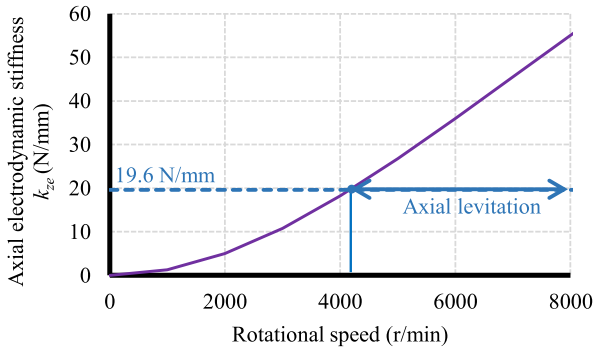

FIGURE 7. Axial electrodynamic stiffness plot calculated through FEA and the threshold for axial electrodynamic suspension.

TABLE 3. Parameters Estimated for the Radial Permanent Magnet Bearing

k_{zp}	d_o	Min. k_{ze}	Min. ω
-5.66 N/mm	1 mm	19.62 N/mm	4200 r/min

Substituting k_{zp} in (12), it is possible to estimate the minimum rotational speed required for achieving axial suspension. The rotor mass m is 2 kg and the lower touchdown position z_t is -1 mm. Per mechanical design d_o is set to 1 mm. The minimum k_{ze} for axial suspension is, thus, estimated as 19.62 N/mm. Fig. 7 shows the plot of axial stiffness calculated through (5) along with the axial suspension threshold. From the figure, it is estimated that the rotor shaft will become axially suspended around 4200 r/min. The radial bearing parameters are given in Table 3.

IV. EXPERIMENTAL PROCEDURE

A. DESCRIPTION OF THE EXPERIMENTAL SETUP

An experiment was conducted to verify the passive axial electrodynamic suspension in the bearingless motor. A 3-D model of the experimental setup is shown in Fig. 8. Besides the bearingless motor and the radial permanent magnet bearings described earlier, there are a few supporting structures included in the setup.

Two radial ball bearings are mounted on the frame. They act as touchdown bearings and restrict the maximum displacement of the rotor shaft. The maximum axial displacement is ± 1 mm. The maximum radial displacement is 0.5 mm.

There is a laser sensor IL-030 by Keyence attached to the base. The sensor is used to assess the axial position and confirm the passive suspension. It is not used for any form of closed-loop control. The target of the laser sensor is the hexagonal head of the lower rotor bolt. The head of the bolt is flat, smooth, and reflective.

Around the upper end of the rotor shaft, there is a 3-D-printed support that houses four Hall sensors. These Hall sensors face a two-pole permanent magnet ring attached to the upper end of the rotor shaft. The rotor angular position is calculated from the Hall sensor outputs and used in the feedback control of rotor rotational speed. There are two sensors facing opposite directions on both the x- and y-axes. The output

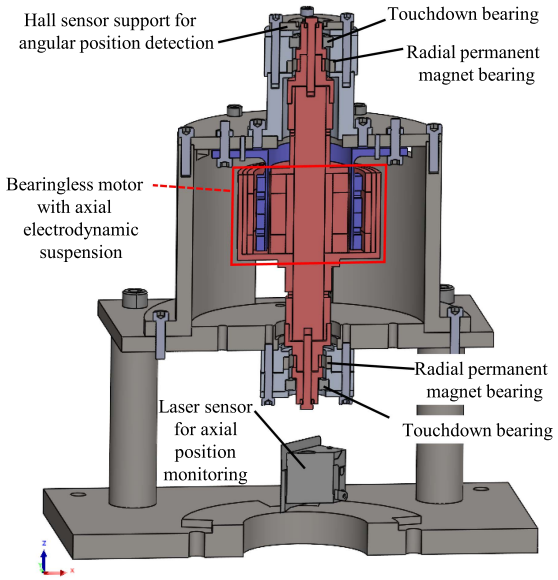

FIGURE 8. 3-D model of the experimental setup used in the verification of axial electrodynamic suspension. Besides the bearingless motor and radial permanent magnet bearings, there are touchdown ball bearings, Hall sensors for angular position detection, and a laser sensor for axial position monitoring.

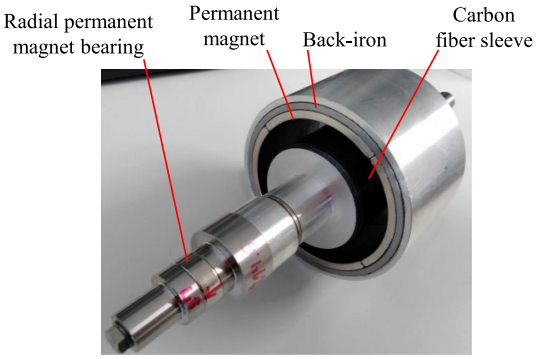

FIGURE 9. Rotor of the bearingless motor with electrodynamic suspension. The rotor has an inner and an outer parts that embrace the stator coils.

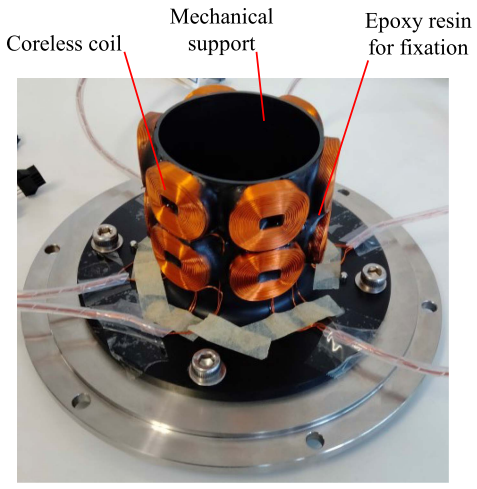

FIGURE 10. Stator coils. The coils are fixed with epoxy resin to the mechanical support.

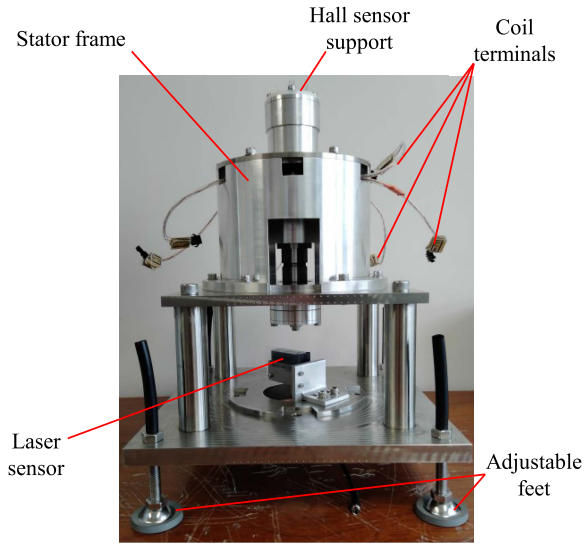

FIGURE 11. Picture of the experimental setup. The stator coils and sensors are disconnected from their respective power sources in the picture.

signal from these opposing sensors is averaged to compensate for the radial displacement. The output signals are previously calibrated and normalized to eliminate variations in amplitude and offset. The control algorithm also compensates for the angular displacement between the sensor permanent magnet and the magnetic rotor pole.

The machine is driven at constant rotational speed by a feedback control loop. Up to the threshold speed for axial suspension, the rotor sits on the lower touchdown ball bearing. Above the minimum speed, the rotor is expected to lift.

Fig. 9 shows a picture of the rotor. It is composed of an inner and an outer parts that are mechanically connected by an aluminum frame. There are, in total, 24 neodymium N50 segmented permanent magnets, 12 on the inner part and 12 on the outer part. There are SS400 back-iron behind the permanent magnets on both the inner and outer rotor parts. The inner permanent magnets are retained by a carbon fiber sleeve. Figs. 10 and 11 show, respectively, pictures of the stator coils and the experimental setup. The coreless coils are fixed to the mechanical support with epoxy resin.

B. FINDING THE AXIAL POSITION OF THE MAGNETIC CENTER

During the first experiment, it was noticed that there was a significant asymmetry between the motor current supplied by the inverter at lower and upper touchdown positions. Since the coil connections were correct, this asymmetry indicated a significant displacement between the magnetic center and the middle point between the upper and lower touchdown bearings.

From (7), it is known that the braking torque due to the axial suspension current is proportional to the square of axial

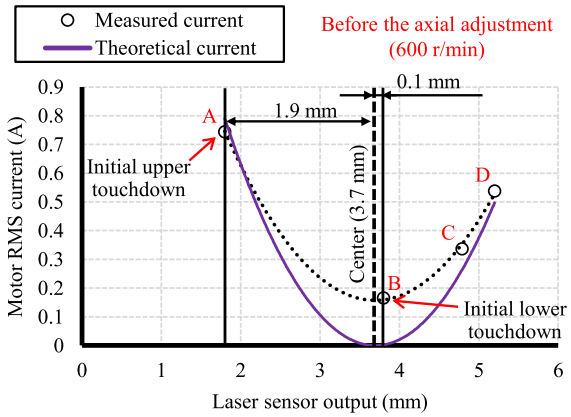

FIGURE 12. Motor currents on phase *A* measured in lower and upper touchdown positions at a constant rotational speed of 600 r/min. Additional axial positions C and D, below the lower touchdown, were achieved by shifting the lower touchdown bearing downward by inserting laminated steel sheets.

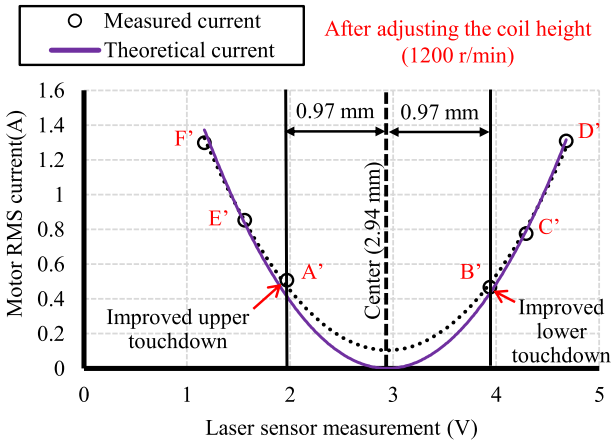

FIGURE 13. Motor rms currents on phase *A* at lower and upper touchdown positions after correcting the mismatch between the magnetic center and the middle point between upper and lower mechanical touchdown. The rms currents were measured at constant rotational speed of 1200 r/min. Positions C′, D′, E′, and F′, beyond the initial touchdown, were obtained by shifting the touchdown bearings by inserting laminated steel sheets.

position z. Since the motor torque is proportional to the motor rms current, if the rotor is kept at constant rotational speed, it is possible to determine the central axial position by finding the axial position where the motor current is minimum.

Fig. 12 shows the motor rms currents measured at upper and lower touchdown conditions at constant rotational speed 600 r/min. The inverter current i_a is measured in the position indicated by current clamp 2 in Fig. 3. The points A and B in the plot correspond to the standard touchdown positions, 3.8 and 1.8 mm, respectively, as indicated by absolute measurements of the laser sensor. By inserting laminated steel sheets between the bearing support and the experiment frame, the touchdown was axially shifted and the current was measured at two additional positions C and D. Through second degree fitting, an equation for motor current in terms of the laser sensor output was derived. Differently from (7), zero current is not achieved at the estimated central axial position due to axial misalignment between the figure-eight coils. The axial misalignment between the coils is investigated in the back-EMF measurements of Section IV-C. Owing to this misalignment, the neutral axial position where circulating suspension current is zero is different among the figure-eight coil sets. However, the origin of the z-axis can be set for absolute minimum braking torque. In other words, it can be found by calculating the position where the derivative of the fitted motor current curve is equal to zero. The estimated position for the magnetic center is 3.7 mm as indicated by the laser sensor. It was 0.1 mm above the lower touchdown and 1.9 mm below the upper touchdown positions. In this condition, if the machine is started in lower touchdown, the axial displacement z is too small; thus, there is not enough axial force to lift the rotor and reach noncontact suspension. If the machine is started in upper touchdown, the initial displacement and, consequently, the braking torque are higher than that of the lower touchdown condition.

To adjust the axial displacement, the stator coil was shifted 0.9 mm upward with respect to the initial position. It was moved farther from the lower touchdown ball bearing and closer to the upper one. Fig. 13 shows the motor currents measured after the adjustment. The currents were measured both in upper and lower touchdown positions, A' and B', respectively, at constant rotational speed 1200 r/min. Additional measurements, C', D', E', and F', were carried out after shifting the touchdown bearings by inserting laminated steel sheets. The minimum motor current now occurs at 2.94 mm, as measured by the laser sensor. The upper and lower touchdowns are 0.97 mm away from the center, indicating that the mechanical adjustment was successful and the magnetic center of the bearingless motor is aligned with the middle point between upper and lower touchdown positions.

C. MEASUREMENT OF BACK-EMF

By cutting the parallel connection between the upper and lower coils, it is possible to drive this machine with only half winding while the other half is open, as shown in the circuit diagram in Fig. 14. This configuration permits measuring directly the back-EMF induced in the coils with open terminals. This connection is used only for assessing the back-EMF. It is not used during the other experiments.

An experiment was carried out to assess the back-EMF of each phase at constant 1200 r/min rotational speed at several fixed axial positions z. First, the upper coils were fed by the inverter while the lower coils had one open terminal, as shown in Fig. 14. All coils were in a star connection with common neutral point. The voltages V_{al}, V_{bl}, and V_{cl}, measured between the open coil terminals and the neutral point, are equal to the sum of back-EMF in the lower coils for each phase. In a similar fashion, voltages V_{au}, V_{bu}, and V_{cu} were measured by disconnecting the phase terminals from the upper coils and driving the rotor with the lower coils. Fig. 15(a) shows the back-EMF measured in the lower coils at lower touchdown

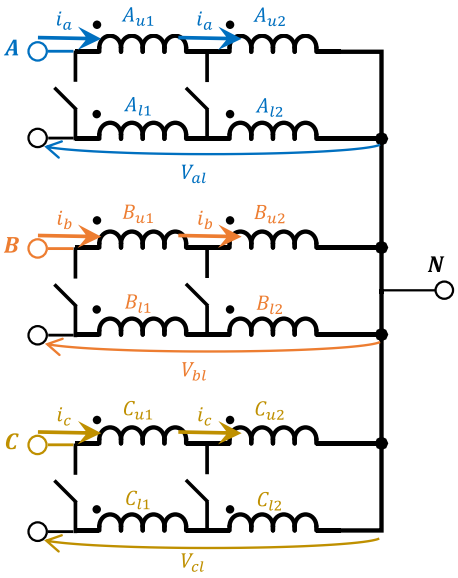

FIGURE 14. Circuit diagram of the experiment for measuring the back-EMF. The upper coils are fed by a regulated motor current that drives the machine at constant rotational speed. Back-EMF in the lower coils is measured with oscilloscope probes connected between the open terminal and the neutral point. Back-EMF in the upper coils can be measured by connecting the lower coils to the inverter and opening the upper coil terminals.

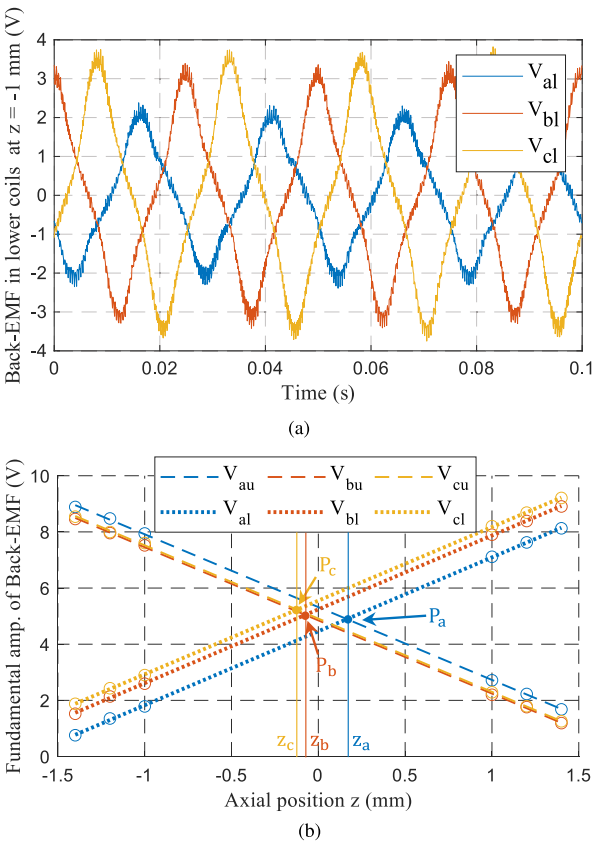

FIGURE 15. Back-EMF measured at constant 1200 r/min rotational speed. The first-degree polynomial fit of the amplitude can be used to characterize the axial misalignment between the figure-eight coils. (a) Back-EMF for phases *A*, *B*, and *C* at z = −1 mm. (b) Amplitude of the fundamental harmonic component of back-EMF at several axial positions.

position $z = -1$ mm. A discrepancy is observed among the amplitudes of the back-EMF of the three phases, indicating a misalignment between the neutral magnetic center of the coils.

Fig. 15(b) shows the first-degree polynomial fit of the amplitude of the fundamental harmonic component of back-EMF for the upper and lower coils at axial positions −1.4, −1.2, −1, 1, 1.2, and 1.4 mm. Displacements beyond the standard axial touchdown positions $z = 1$ mm and $z = -1$ mm were achieved by mechanically offsetting parts of the experimental setup using laminated steel sheets with 0.2 mm thickness. This procedure is similar to that of Section IV-B. The back-EMF is a first-degree function of axial position z, as derived in (2). Therefore, it is possible to calculate the constant K_λ through first-degree fitting of the back-EMF curves. Moreover, the crossing points of the upper and lower back-EMF amplitude curves, P_a, P_b, and P_c, are equivalent to the magnetic center of each phase [27]. P_a, P_b, and P_c are positioned at $z_a = 0.16$ mm, $z_b = -0.07$ mm, and $z_c = -0.12$ mm, respectively. This result explains why the minimum motor current in Figs. 12 and 13 is not zero.

The average ratio K_λ for the whole winding is derived as

$$K_\lambda = \frac{d}{dz}\left(\frac{V_{al} + V_{bl} + V_{cl} - V_{au} - V_{bu} - V_{cu}}{12}\right). \quad (16)$$

The experimental value of K_λ was calculated as 5.2 Wb/m, 5% lower than that estimated with FEA.

D. AXIAL SUSPENSION AND MOTOR CURRENT RESULTS

Currents and axial positions were measured for constant rotational speeds up to 8065 r/min. Total coil current i_{al1} in coil A_{l1} and the motor current i_a were measured with current clamp probes, as indicated in Fig. 3. The axial position was monitored by a laser sensor.

Fig. 16(a) shows the axial position measured with the laser sensor at constant speeds 0 and 8065 r/min. The plotted axial position was calculated as the displacement from the magnetic center characterized in Fig. 13. With a static rotor sitting on the lower touchdown bearing, the measured axial position was −0.99 mm. At 8065 r/min, the average measured axial position was $z = -0.28$ mm with 15.4% ripple.

Fig. 16(b) shows the currents measured at 8065 r/min. The experimental suspension current was not directly measured. Its instantaneous value was calculated as $i_{za1} = i_a/2 - i_{al1}$. There is a current peak variation observed every two mechanical cycles. This variation may be caused by radial displacement or precession of the rotor shaft.

Fig. 17(a) shows a comparison between the experimental and theoretical results for steady state equilibrium axial position z at several rotational speeds. The markers in the measured position plot are the average measurements of the laser sensor outputs. The error bars are equivalent to the peak-to-peak values measured by the oscilloscope. There is a reasonable correspondence. The theoretical values of steady-state axial position z were calculated with $K_\lambda = 5.2$˜Wb/m, obtained from the back-EMF experiment. The rotor was expected to reach axial suspension around 4450 r/min; however,

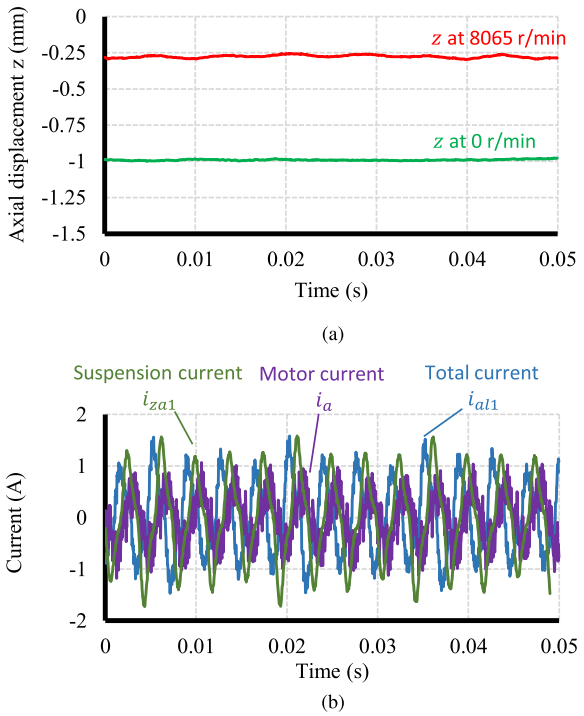

FIGURE 16. Currents and axial position measured in the experiment with an oscilloscope. The axial position is measured from the analog output signal of the laser sensor. The suspension current has a low-frequency variation probably due to radial movement and rotor precession. (a) Axial position measured at 0 speed and at 8065 r/min. (b) Currents measured at 8065 r/min.

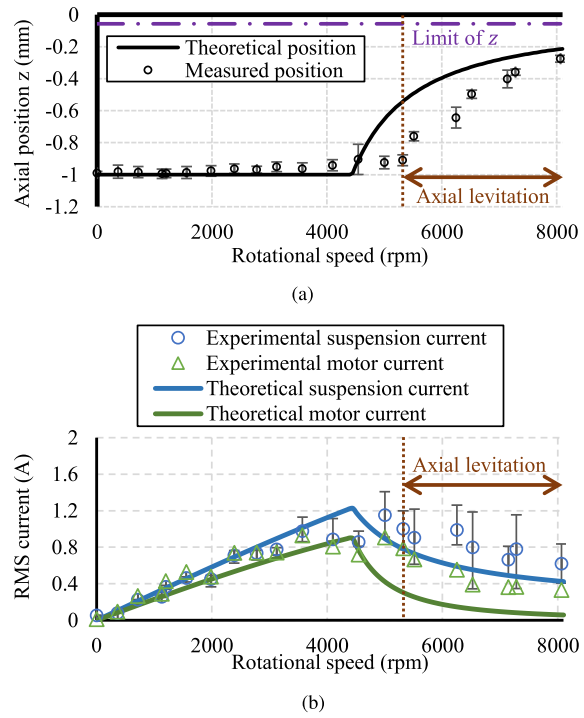

FIGURE 17. Axial position, motor and suspension rms currents for rotational speeds up to 8065 r/min. (a) Axial position variation with rotational speed. (b) RMS currents variation with rotational speed.

in the experiment, suspension was only confirmed above 5319 r/min. This difference is attributed to uncertainty of parameters in the radial permanent magnet bearings, such as assembly error in the axial offset d_o. There is a tilting angle between the rotor and the vertical direction, because a precession movement was observed. This inclination slightly decreases the resultant axial electrodynamic force. Assuming that d_o is smaller than the design specification, the static axial load $mg - F_o$ is increased, resulting in a higher rotational speed requirement for axial suspension, even if the mechanical error is of the order of 0.1 mm.

Fig. 17(b) shows the measured motor and suspension rms values of the fundamental current components. The currents were measured at rotational speeds up to 8065 r/min. The plot also shows the respective theoretical currents for each speed. The theoretical suspension current was calculated by dividing the amplitude of (3) by $\sqrt{2}$, whereas the rms motor current was estimated by dividing (7) by the torque–current factor $k_T = 0.0796$ Nm/A. There are error bars plotted for the experimental suspension current values, because the suspension current amplitude varies every few mechanical cycles, as shown in Fig. 16(b). Up to 5319 r/min, the motor rms current increases because of the braking torque caused by the suspension current. The motor current reaches a peak during the transition to axial suspension and falls from about 1.15 A to 0.62 A. The measured current did not get as close to zero as the theoretical value because of the difference observed in the axial equilibrium position depicted in Fig. 17(a). There may also be unaccounted losses, such as those from the third harmonic component of the suspension current, pulsewidth modulation harmonics, proximity effect, and eddy currents on the cross section of the coil conductors and surface of the permanent magnets.

V. CONCLUSION

This article covered a surface-mounted permanent magnet bearingless motor with passive axial electrodynamic suspension and passive radial permanent magnet bearings.

The electrodynamic suspension principle was described. Equations for the braking torque and steady-state axial equilibrium position were derived. The electrodynamic stiffness increases with rotational speed; therefore, it must overcome a minimum speed threshold to achieve axial suspension. This threshold depends on parameters, such as the rotor weight, touchdown position, and the stiffness of the radial permanent magnet bearings. Both the suspension current and braking torque are proportional to the square of the axial displacement z. The passive radial permanent magnet bearing was described, and the minimum rotational speed for achieving passive axial suspension was estimated

A method was proposed to compensate for the misalignment between the middle point between upper and lower touchdowns and the magnetic center where suspension current is minimum.

Axial suspension was confirmed for rotational speeds above 5319 r/min. The minimum speed for levitation observed during the experiment was higher than the preliminary estimation of 4200 r/min, calculated through (5) and (12) with a $K_\lambda = 5.5$ Wb/m obtained through FEA. It was also higher than 4450 r/min, and the minimum speed estimated with the corrected $K_\lambda = 5.2$ Wb/m was obtained from the back-EMF experiment. This difference is attributed to the uncertainty of the offset axial force F_o in the radial permanent magnet bearings and a precession movement observed during suspension.

ACKNOWLEDGMENT

The authors would like to thank JSOL Corporation for the educational license of JMAG software.

REFERENCES

[1] M. Osa, T. Masuzawa, R. Orihara, and E. Tatsumi, "Compact maglev motor with full DOF active control for miniaturized rotary blood pumps," in *Proc. 11th Int. Symp. Linear Drives Ind. Appl.*, 2017, pp. 1–6.
[2] M. Bleuler et al., "Micromachined active magnetic bearings," in *Proc. 4th Int. Symp. Magn. Bearings*, 1994, pp. 349–352.
[3] R. Schoeb and N. Barletta, "Principle and application of a bearingless slice motor," *JSME Int. J., Ser. C: Mech. Syst., Mach. Elements Manuf.*, vol. 40, no. 4, pp. 593–598, 1997.
[4] T. Schneeberger, T. Nussbaumer, and J. W. Kolar, "Magnetically levitated homopolar hollow-shaft motor," *IEEE/ASME Trans. Mechatronics*, vol. 15, no. 1, pp. 97–107, Feb. 2010.
[5] H. Mitterhofer and W. Amrhein, "Design aspects and test results of a high speed bearingless drive," in *Proc. Int. Conf. Power Electron. Drive Syst.*, 2011, pp. 705–710.
[6] S. Yang and M. Huang, "Design and implementation of a magnetically levitated single-axis controlled axial blood pump," *IEEE Trans. Ind. Electron.*, vol. 56, no. 6, pp. 2213–2219, Jun. 2009.
[7] J. Asama, Y. Hamasaki, T. Oiwa, and A. Chiba, "Proposal and analysis of a novel single-drive bearingless motor," *IEEE Trans. Ind. Electron.*, vol. 60, no. 1, pp. 129–138, Jan. 2013.
[8] W. Bauer and W. Amrhein, "Electrical design considerations for a bearingless axial-force/torque motor," *IEEE Trans. Ind. Appl.*, vol. 50, no. 4, pp. 2512–2522, Jul./Aug. 2014.
[9] H. Sugimoto and A. Chiba, "Parameter identification of current–force factor and torque constant in single-drive bearingless motors with back EMF," *IEEE Trans. Ind. Appl.*, vol. 55, no. 5, pp. 4754–4761, Sep./Oct. 2019.
[10] W. Gruber, H. Grabner, S. Silber, and W. Amrhein, "Design of a brushless permanent-magnet synchronous drive with a purely passively suspended rotor," *IEEE Trans. Ind. Appl.*, vol. 50, no. 5, pp. 3258–3264, Sep./Oct. 2014.
[11] E. Rodriguez et al., "Analysis of passive magnetic bearings for kinetic energy storage systems," in *Proc. 14th Int. Symp. Magn. Bearings*, 2014, pp. 11–14.
[12] Q. Cui, J. Sandtner, and H. Bleuler, "Whirl imposer: Proposal for a novel passive magnetic rotor bearing system," in *Proc. 14th Int. Symp. Magn. Bearings*, 2014, pp. 606–610.
[13] Y. Xu, Q. Cui, R. Kan, H. Bleuler, and J. Zhou, "Realization of a diamagnetically levitating rotor driven by electrostatic field," *IEEE/ASME Trans. Mechatronics*, vol. 22, no. 5, pp. 2387–2391, Oct. 2017.
[14] R. F. Post, "Dynamically stable magnetic suspension/bearing system," U.S. Patent 5,495,221, issued Feb. 27, 1996.
[15] A. V. Filatov and E. H. Maslen, "Passive magnetic bearing for flywheel energy storage systems," *IEEE Trans. Magn.*, vol. 37, no. 6, pp. 3913–3924, Nov. 2001.
[16] A. Filatov, "'Null-e' magnetic bearings," Ph.D. dissertation, University of Virginia, Charlottesville, VA, USA, 2002.
[17] J. Sandtner and H. Bleuler, "Electrodynamic passive magnetic bearing with planar halbach arrays," in *Proc. 9th Int. Symp. Magn. Bearings*, 2004, pp. 3–6.
[18] T. A. Lembke, "Design and analysis of a novel low loss homopolar electrodynamic bearing," Ph.D. dissertation, KTH Royal Institute of Technology, Stockholm, Sweden, 2005.
[19] A. Tonoli, N. Amati, F. Impinna, and J. G. Detoni, "A solution for the stabilization of electrodynamic bearings: Modeling and experimental validation," *J. Vib. Acoust.*, vol. 133, no. 2, 2011, Art. no. 021004.
[20] K. D. Bachovchin, J. F. Hoburg, and R. F. Post, "Stable levitation of a passive magnetic bearing," *IEEE Trans. Magn.*, vol. 49, no. 1, pp. 609–617, Jan. 2013.
[21] F. Impinna, J. G. Detoni, N. Amati, and A. Tonoli, "Passive magnetic levitation of rotors on axial electrodynamic bearings," *IEEE Trans. Magn.*, vol. 49, no. 1, pp. 599–608, Jan. 2013.
[22] C. Dumont, V. Kluyskens, and B. Dehez, "Linear state-space representation of heteropolar electrodynamic bearings with radial magnetic field," *IEEE Trans. Magn.*, vol. 52, no. 1, Jan. 2016, Art. no. 8100109.
[23] H. Matsue, "Electromagnetic property of bearingless motor based on electro-magnetic induction," *Railway Tech. Res. Inst. Rep.*, vol. 25, no. 3, pp. 47–52, 2011.
[24] J. V. Verdeghem, V. Kluyskens, and B. Dehez, "Five degrees of freedom linear state-space representation of electrodynamic thrust bearings," *J. Sound Vib.*, vol. 405, pp. 48–67, Sep. 2017.
[25] V. Kluyskens, J. Van Verdeghem, and B. Dehez, "Experimental investigations on self-bearing motors with combined torque and electrodynamic bearing windings," *Actuators*, vol. 8, no. 2, Jun. 2019, Art. no. 48. [Online]. Available: https://www.mdpi.com/2076-0825/8/2/48
[26] J. Van Verdeghem, M. Lefebvre, V. Kluyskens, and B. Dehez, "Dynamical modeling of passively levitated electrodynamic thrust self-bearing machines," *IEEE Trans. Ind. Appl.*, vol. 55, no. 2, pp. 1447–1460, Mar./Apr. 2019.
[27] J. Van Verdeghem, V. Kluyskens, and B. Dehez, "Experimental investigations on passively levitated electrodynamic thrust self-bearing motors," *IEEE Trans. Ind. Appl.*, vol. 55, no. 5, pp. 4743–4753, Sep./Oct. 2019.
[28] B. Dehez, C. D. de Chassart, J. Van Verdeghem, and V. Kluyskens, "Electric machine having an axial electrodynamic bearing," U.S. Patent Application 16/609,337, 2020.
[29] J. Van Verdeghem and B. Dehez, "Fully passively levitated self-bearing machines with combined windings," in *Proc. IEEE Energy Convers. Congr. Expo.*, 2020, pp. 254–261.
[30] J. Van Verdeghem, E. L. Severson, and B. Dehez, "Hybrid active–passive actuation approach of passively levitated thrust self-bearing machines," *IEEE Trans. Ind. Appl.*, vol. 57, no. 6, pp. 7035–7045, Nov./Dec. 2021.
[31] J. Van Verdeghem and B. Dehez, "Fully passively levitated self-bearing machine implemented within a reaction wheel," *IEEE Trans. Ind. Appl.*, vol. 57, no. 6, pp. 5782–5795, Nov./Dec. 2021.
[32] G. C. Rubio and A. Chiba, "Design and analysis of a bearingless motor with passive axial suspension through null-flux coils," in *Proc. IEEE Int. Electric Machines Drives Conf.*, 2019, pp. 779–786.
[33] G. Cavalcante Rubio, Y. Fujii, and A. Chiba, "A bearingless motor with passive electrodynamic suspension in axial direction," *IEEE Trans. Ind. Appl.*, vol. 57, no. 6, pp. 6812–6822, Nov./Dec. 2021.
[34] G. C. Rubio, Y. Fujii, and A. Chiba, "Requirements for full passive suspension on a bearingless motor with electrodynamic axial stabilization and radial permanent magnet bearings," in *Proc. IEEE Energy Convers. Congr. Expo.*, 2021, pp. 3936–3942.
[35] G. Cavalcante Rubio, Y. Fujii, and A. Chiba, "Bearingless motor with asymmetric axial electrodynamic stabilization," in *Proc. Joint Tech. Meeting Magnetics/Motor Drive/Linear Drives*, 2021, pp. 89–94.
[36] J. R. Powell and G. T. Danby, "Magnetic suspension for levitated tracked vehicles," *Cryogenics*, vol. 11, no. 3, pp. 192–204, 1971. [Online]. Available: https://www.sciencedirect.com/science/article/pii/0011227571903110
[37] K. R. Davey, "Designing with null flux coils," *IEEE Trans. Magn.*, vol. 33, no. 5, pp. 4327–4334, Sep. 1977.
[38] K. Sawada, "Development of magnetically levitated high speed transport system in Japan," *IEEE Trans. Magn.*, vol. 32, no. 4, pp. 2230–2235, Jul. 1996.
[39] T. Yonezu, K. Watanabe, E. Suzuki, and T. Sasakawa, "Study on electromagnetic force characteristics acting on levitation/guidance coils of a superconducting maglev vehicle system," *IEEE Trans. Magn.*, vol. 53, no. 11, Nov. 2017, Art. no. 8300605.